2007 IET Seminar on Antennas and Propagation for Body-Centric Wireless Communications, 24-24 April 2007 Page(s):90 - 96

Analytical Propagation Models for Body Area Networks

Gemma Roqueta[1], Andrew Fort[2,3], Christophe Craeye[4], Claude Oestges[4]

[1]Universitat Politècnica de Catalunya (UPC)
Jordi Girona 31
08034 Barcelona, Spain
Email: gemma.roqueta@gmail.com

[2]IMEC, Kapeldreef 75
B-3001 Leuven, Belgium
Email: forta@imec.be
+32.16.28.82.80

[3]Vrije Universiteit Brussel (VUB)
Dept. ELEC
Pleinlaan 2
B-1050 Brussel,Belgium

[4]Université catholique de Louvain (UCL)
Place du Levant 2
B-1348 Louvain-La-Neuve, Belgium
craeye@tele.ucl.ac.be
oestges@emic.ucl.ac.be

Keywords - Body area networks, propagation model

***Abstract*— Using wireless sensors worn on the body to monitor health information is a promising new application. To realize transceivers targeted for these applications, it is essential to understand the body area propagation channel. Several numerical, simulated, and measured body area propagation studies have recently been conducted. While many of these studies are useful for evaluating communication systems, they do not directly consider physical propagation mechanisms forcing researchers to rely on ad-hoc modeling approaches that are not always motivated by fundamental electromagnetic principles. This can result in less insight into expected propagation trends and inappropriate modeling choices. To address this problem, we have developed a simple and generic body area propagation model derived directly from Maxwell's equations. We then verify the resulting analytical model by comparing it with measurements around a body in an anechoic chamber. This paper describes the analytical derivation of this model and compares it with measurements of the electric field close to the body.**

I. Introduction

Wireless bio-medical sensors are a promising new application made possible by recent advances in ultra low power technology [1]. Each sensor measures parameters of interest and sends the data in short bursts to a central device, such as a PDA. Both the sensors and the PDA are worn directly on the body. Examples include sensors to observe brain activity for recording or warning against seizure events, or sensors to examine heart activity for diagnosis and automatic emergency calls. The large diversity and potential of these applications makes it an exciting new research direction.

In order to develop efficient low power radio systems for use near the human body, we require simple and generic body area propagation models. Measurements [2]–[5] and Finite Difference Time Domain (FDTD) simulations [6]–[8] have successfully described very specific communication scenarios. Using measured or simulated results, complete statistical ultra-wideband models have been developed in [9], [10] and standardized by the IEEE [11]. Some of these approaches have already proven effective for evaluating body area communication system proposals [12], [13]. However, measurements and simulation do not directly consider the physical propagation mechanism, forcing researchers to rely on some ad-hoc modeling approaches that are not always motivated by fundamental principles. This can result in less insight into expected propagation trends and inappropriate modeling choices. Another approach is to use the Uniform Theory of Diffraction (UTD) [14]. UTD is an extension to ray tracing allowing the propagation channel to be described in terms of the sum of rays diffracting around and reflecting off of body parts [8]. While this approach offers considerable physical insight, it typically relies on a high-frequency asymptotic approximation which is not valid at low frequencies, or for tangentially polarized antennas placed very close to the human body [14]. This scenario is particularly important for body worn antennas which must be low-profile and therefore polarized tangent to the body in practice.

In order to better understand physical propagation trends near the body, we have developed a simple but generic approach to body area propagation derived directly from Maxwell's equations. This approach is valid regardless of the distance of the antenna from the body and can be extended for arbitrary antenna polarity and frequency. We begin by developing the solution for an infinite line source in the vicinity of an infinite lossy cylinder, based on the addition theorem for Hankel functions. We then numerically calculate the inverse Fourier transform of the line source to obtain the fields due to a point source, representing the antenna, near a lossy cylinder, representing the body. Finally, we have validated this approach by comparing the fields predicted by this simple model with actual measurements around the human body in an anechoic chamber.

This article summarizes our approach to analytical body area propagation modeling. Section II begins by outlining the various steps in our analytical developments. This outline serves as a generic recipe which can be applied for different antenna polarizations. To demonstrate this approach, section III reviews the well-known solution for a line-source near a lossy conductor focusing on the specific case of a vertically polarized current source. In the exact solution, the Transverse Electric (TE) and Transverse Magnetic (TM) waves are cou-

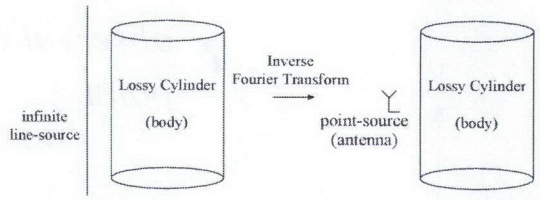

Fig. 1. Proposed two-step procedure for body area modeling. First we obtain the solution for a line-source near a lossy cylinder. Second, we transform the solution to a point source by taking its inverse Fourier transform.

pled upon scattering by the cylinder [15]. We will omit this coupling in our analysis by neglecting the small $\hat{\phi}$ components of the scattered and incident fields. This simplifies the mathematics while providing an adequate approximation of the exact solution. To obtain a realistic model of a very small antenna close to the body, Section IV performs a numerical integration to transform the line source into a point source. Section V then compares the resulting model with measurements taken near a body in an anechoic chamber. Finally, Section VI summarizes the major conclusions of this study.

II. Generic approach to body area modeling

Figure 1 summarizes our proposed approach to body area modeling. We model the antennas as a point source with some polarity, and the human body as an infinite lossy cylinder with arbitrary material parameters. A point source is a reasonable approximation of an antenna if the antenna size is small compared with the wavelength. This is normally the case for compact body-worn devices. A lossy cylinder is a reasonable first order approximation of a human body allowing us to take into account many propagation phenomenon including diffraction around a curved lossy surface, reflections off the body, and penetration into the body. All of these effects are expected to play a role in body area propagation, though the relative importance of each effect will depend on such factors as the frequency, polarity, radius of curvature, and tissue properties. Thus, our chosen geometry will allow us to explore many important body area propagation phenomenon while still remaining analytically tractable so that a solution can be derived directly from fundamental principles.

In order to derive the electric fields around and inside a lossy cylinder resulting from a point source, we follow a two step procedure as indicated in Figure 1. First, we solve the problem of a linear current source located outside a lossy cylinder. The solution to this problem can be obtained by using the well known addition theorem for Hankel functions to represent the displaced cylindrical waves of the line source by a superposition of un-displaced cylindrical waves originating from the origin. This allows us to easily enforce the boundary conditions around the surface of our lossy cylinder. Section III describes the details of this step. Second, we convert the line source to a point source by performing an inverse Fourier transform of the current source along the vertical spectral coordinate (k_z). This approach takes advantage of the fact that the point source represented by the dirac function $\delta(z - z_0)$ and a line source represented by $e^{-jk_z(z+z_0)}$ are Fourier transform pairs. The transform must be obtained numerically using a contour integral to avoid a singularity in the line source solution. Section IV describes the details of this step.

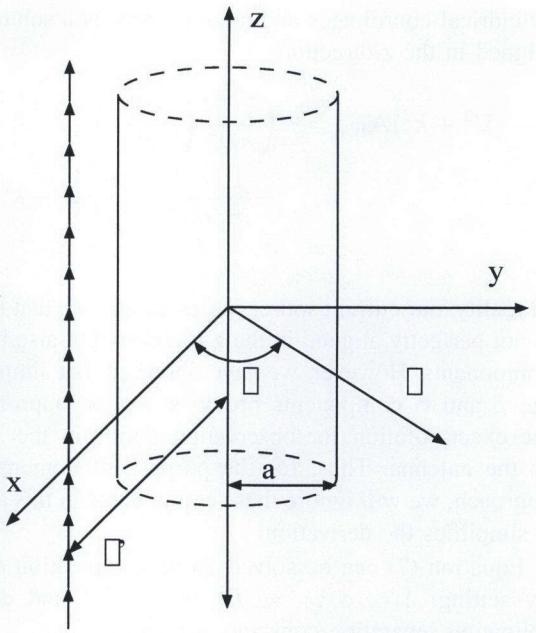

Fig. 2. Geometry and coordinate system for our analysis

Throughout this article, we focus on the special case of a vertically polarized point source, but the general approach can be repeated for other polarities.

III. Line Source

Figure 2 provides a more precise diagram of our geometry emphasizing the major variables used throughout our analysis. An infinite cylinder of radius a is oriented along the z-axis at the origin of our coordinate system. An infinite linear current source is located at cylindrical coordinates (ρ', ϕ'). We begin by deriving the solution of the non-homogeneous wave equation linking the current and the magnetic vector potential:

$$(\nabla^2 + k^2)\mathbf{A} = -e^{-jk_z z}\delta(x - x')\delta(y - y') \qquad (1)$$

The right hand side of this equation represents a z-directed conducting line source at position (x', y'). The term $e^{-jk_z z}$ indicates that the current along this line is a traveling wave with a vertical propagation constant k_z. This choice of current will allow us to convert it to a point source by means of an inverse Fourier transform in Section IV.

The general solution to this differential equation can be written as the sum of the solution to the homogeneous equation $(\nabla^2 + k^2)\mathbf{A_h} = 0$, and any particular solution to equation (1). The homogeneous solution corresponds physically to the scattered field due to charges on the surface of the cylinder. The particular solution corresponds to the incident field from the line source propagating through free space without the presence of the lossy cylinder. The scattered and incident fields are described in Sections III-A and III-B respectively. Section III-C describes the total solution obtained by summing the scattered and incident fields and enforcing the boundary conditions along the surface of the cylinder.

A. Scattered field

To obtain the homogeneous solution representing the scattered field, we will expand the homogeneous equation in

cylindrical coordinates and assume there is a solution for $\mathbf{A_h}$ aligned in the z-direction:

$$\begin{aligned}(\nabla^2 + k^2)\mathbf{A_h} &= \left(\frac{1}{\rho}\frac{\partial}{\partial\rho}\left(\rho\frac{\partial A_z}{\partial\rho}\right)\right. \\ &\quad \left. + \frac{1}{\rho^2}\frac{\partial^2 A_z}{\partial\phi^2} + \frac{\partial^2 A_z}{\partial z^2} + k^2 A_z\right)\hat{\mathbf{z}} \\ &= 0 \end{aligned} \tag{2}$$

In reality, our current source varies along z so that the solution is not perfectly aligned in the **z**-direction but also has $\hat{\rho}$ and $\hat{\phi}$ components. However, we have observed that simply ignoring the $\hat{\rho}$ and $\hat{\phi}$ components provides a good approximation to the exact solution for observation points in the same plane as the antenna. Thus, for the purpose of demonstrating our approach, we will ignore these components in this article since it simplifies the derivation.

Equation (2) can be solved through separation of variables by setting $A_z(\rho,\phi,z) = R(\rho)\Phi(\phi)Z(s)$ and defining the following separation constants m^2 and k_z^2:

$$\frac{1}{\Phi(\phi)}\frac{\partial^2\Phi(\phi)}{\partial\phi^2} = -m^2 \tag{3}$$

$$\frac{1}{Z(z)}\frac{\partial^2 Z(z)}{\partial z^2} = -k_z^2 \tag{4}$$

These equations together with (2) allow us to write three equations separated in terms of Φ, Z, and R as follows:

$$\frac{\partial^2\Phi(\phi)}{\partial\phi^2} + m^2\Phi(\phi) = 0 \tag{5}$$

$$\frac{\partial^2 Z(z)}{\partial z^2} + k_z^2 Z(z) = 0 \tag{6}$$

$$\rho\frac{\partial}{\partial\rho}\left(\rho\frac{\partial R(\rho)}{\partial\rho}\right) + (\rho^2 k_\rho^2 - m^2)R(\rho) = 0 \tag{7}$$

with

$$k_\rho = \sqrt{k^2 - k_z^2} \tag{8}$$

The solutions of equations (5) and (6) are harmonic functions of the form $\Phi(\phi) = ae^{-jm\phi}$ and $Z(z) = be^{-jk_z z}$ respectively. Equation (7) is a Bessel's equation of order m having a solution that can be written in terms of Hankel and Bessel functions of the form $R(\rho) = cH_m^{(2)}(k_\rho\rho) + dJ_m(k_\rho\rho)$ where $H_m^{(2)}(k_\rho\rho)$ and $J_m(k_\rho\rho)$ represent the Hankel function of the second kind with order m and the Bessel function of the first kind with order m respectively. Since we have set $A_z(\rho,\phi,z) = R(\rho)\Phi(\phi)Z(z)$, the solution for the homogeneous equation is of the following form:

$$\begin{aligned}\mathbf{A}_h(\rho) &= ae^{-jm\phi}be^{-jk_z z}\left(cH_m^{(2)}(k_\rho\rho) + dJ_m(k_\rho\rho)\right)\hat{\mathbf{z}} \\ &= e^{-jm\phi}e^{-jk_z z}\left(a'H_m^{(2)}(k_\rho\rho) + b'J_m(k_\rho\rho)\right)\hat{\mathbf{z}} \end{aligned} \tag{9}$$

The constants a' and b' will be determined from the boundary conditions of our geometry in Section III-C.

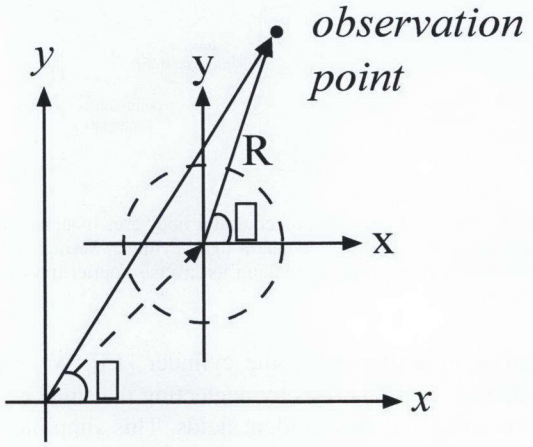

Fig. 3. Displaced cylindrical harmonic and its displaced coordinate system

B. Incident field

It is clear from this geometry that the $\hat{\mathbf{z}}$ component of the electric field radiated by line source will take the form of an outgoing cylindrical traveling wave represented mathematically by a Hankel function of the second kind [15]:

$$\mathbf{A_p}(R) = \frac{e^{-jk_z z}}{4j}H_0^{(2)}(k_\rho R)\hat{\mathbf{z}} \tag{10}$$

where R is the distance from the source to the observation point (see Figure 3). As in Section III-A, we have ignored the $\hat{\phi}$ and $\hat{\rho}$ components of the field to simplify the problem so our resulting expressions will only approximate the exact solution.

When the current source is not centered at the origin, but centered at ρ' it is convenient to use the *addition theorem for Hankel's functions* [16]. This theorem states that a displaced cylindrical wave can be represented by the superposition of un-displayed cylindrical harmonics (see Figure 3). This representation will help us in Section III-C to enforce the boundary conditions along the surface of the cylinder. The addition theorem for Hankel's functions can be represented mathematically as follows:

$$H_0^{(2)}(k_\rho R) = \begin{cases} \sum_{m=-\infty}^{+\infty} J_m(k_\rho\rho)H_m^{(2)}(k_\rho\rho')e^{jm(\phi-\phi')} & \rho \le \rho' \\ \sum_{m=-\infty}^{+\infty} J_m(k_\rho\rho')H_m^{(2)}(k_\rho\rho)e^{jm(\phi-\phi')} & \rho \ge \rho' \end{cases} \tag{11}$$

This can be substituted directly into equation (10) to obtain the particular solution $\mathbf{A_p}(\rho)$ in terms of un-displaced cylindrical harmonics.

C. Total field

The complete solution to the non-homogeneous solution is the sum of the homogeneous and particular solutions obtained in Sections III-A and III-B respectively:

$$\mathbf{A_{TOT}}(\rho) = \mathbf{A_h}(\rho) + \mathbf{A_p}(\rho) \tag{12}$$

Combining this with equations (9) and (10) together with the addition theorem from equation (11) allows us to write the total solution as follows:

$$\mathbf{A_{TOT}}(\rho) = \frac{e^{-jk_z z}}{4j}\sum_{m=-\infty}^{+\infty} e^{jm(\phi-\phi')}R_m(k_\rho\rho)\hat{\mathbf{z}} \tag{13}$$

$$R_m(k_\rho R) = \begin{cases} J_m(k_{\rho 1}\rho)A_m & \rho \le a \\ J_m(k_{\rho 2}\rho_2)H_m^{(2)}(k_{\rho 2}\rho') + H_m^{(2)}(k_{\rho 2}\rho)B_m & a \le \rho \le \rho' \\ J_m(k_{\rho 2}\rho')H_m^{(2)}(k_{\rho 2}\rho) + H_m^{(2)}(k_{\rho 2}\rho)B_m & \rho \ge \rho' \end{cases} \quad (14)$$

$$k_2^2 = \omega^2 \epsilon_0 \mu_0 \quad (15)$$

$$k_1^2 = \omega^2 \epsilon_0 \epsilon_1 \mu_0 \mu_1 \quad (16)$$

$$k_{\rho 2}^2 + k_z^2 = k_2^2 \quad (17)$$

In equation (14), we note that the homogeneous solution inside the cylinder ($\rho \le a$) can only contain Bessel functions since the Hankel functions approach infinity at the origin. Physically, this means that the solution inside the cylinder consists of standing waves. The solution between the line source and the cylinder ($a \le \rho \le \rho'$) contains both Bessel and Hankel functions. The solution beyond the source, ($\rho \ge \rho'$) consists only of Hankel functions since Bessel functions approach infinity for large complex arguments. Physically, this means that the solution outside the cylinder contains outward traveling waves generated from the line-source and charges on the cylinder. The variables k_1 and k_2 represent the wave numbers inside the cylinder and in free-space, respectively. They are defined in terms of the angular frequency (ω), the free-space permittivity (ϵ_0), the free-space permeability (μ_0), and the relative effective permittivity and permeability of the lossy cylinder (ϵ_1 and μ_1 respectively).

To obtain the electric field from the total vector potential, we start with the following two relations:

$$\mathbf{E} = -\nabla V - j\omega \mathbf{A} \quad (18)$$

$$\nabla \cdot \mathbf{A} = -j\omega \epsilon \mu V \quad (19)$$

Equation (18) indicates that the electric field can be written in terms of the scalar electric potential V due to an accumulation of charges, and the vector magnetic potential $\mathbf{A}$ due to a time-varying magnetic field. Equation (19) is the Lorentz condition used to define the vector magnetic potential. Combining these equations with equation (15) gives

$$\mathbf{E} = \frac{1}{j\omega\mu\epsilon}[k^2 + \nabla(\nabla\cdot)]\mathbf{A} \quad (20)$$

Substituting equation (13) into equation (20) yields

$$E_z = \frac{1}{j\omega\mu\epsilon}\frac{1}{4j}k_\rho^2 e^{-jk_z z}\sum_{m=-\infty}^{+\infty} e^{jm(\phi-\phi')}R_m(k_\rho\rho) \quad (21)$$

The magnetic field is obtained directly from the definition of the vector magnetic potential as follows:

$$\mathbf{H} = \frac{1}{\mu}\nabla \times \mathbf{A} \quad (22)$$

Substituting equation (13) into equation (20) yields

$$H_\phi = -\frac{1}{\mu}e^{-jk_z z}\sum_{m=-\infty}^{\infty} e^{jm(\phi-\phi')}R'_m(k_\rho\rho) \quad (23)$$

$$H_\rho = \frac{1}{\mu}e^{-jk_z z}\sum_{m=-\infty}^{\infty} e^{jm(\phi-\phi')}R_m(k_\rho\rho) \quad (24)$$

The boundary conditions can now be applied to determine the constants A_m and B_m. Those conditions state that the tangential components of the electric and magnetic fields are continuous at the surface of the cylinder. Expressed mathematically:

$$E_{z2}(\rho = a) = E_{z1}(\rho = a) \quad (25)$$

$$H_{\phi 2}(\rho = a) = H_{\phi 1}(\rho = a) \quad (26)$$

where E_{z2} and E_{z1} represent the z component of the electric field just outside and just inside the cylinder respectively. Similarly for $H_{\phi 2}$ and $H_{\phi 1}$. Combining equations (25) with (21) allows us to solve for A_m:

$$A_m = \frac{\frac{\mu_2\epsilon_2 k_{\rho 1}^2}{\mu_1\epsilon_1 k_{\rho 2}^2}J_m(k_{\rho 1}a)B_m - J_m(k_{\rho 2}a)H_m^{(2)}(k_{\rho 2}\rho')}{H_m^{(2)}(k_{\rho 2}a)} \quad (27)$$

In a similar manner, a second independent equation can be obtained by combining equations (23), (26), and (27) yielding

$$B_m = \frac{\begin{array}{c} J'_m(k_{\rho 2}a)H_m^{(2)}(k_{\rho 2}\rho')H_m^{(2)}(k_{\rho 2}a) \\ -J_m(k_{\rho 2}a)H_m^{(2)}(k_{\rho 2}\rho')H_m'^{(2)}(k_{\rho 2}\rho) \end{array}}{\begin{array}{c} \frac{k_{\rho 1}\mu_2}{k_{\rho 2}\mu_1}J'_m(k_{\rho 1}a)H_m^{(2)}(k_{\rho 2}a) \\ -\frac{\mu_2\epsilon_2 k_{\rho 1}^2}{\mu_1\epsilon_1 k_{\rho 2}^2}J_m(k_{\rho 1}a)H_m'^{(2)}(k_{\rho 2}a) \end{array}} \quad (28)$$

Equations (27) and (28) may appear complicated, but they can be calculated easily on a computer. To facilitate this computation, we note that the derivatives of Hankel and Bessel functions can be expressed in terms of other Hankel and Bessel functions according to the following well-known relations:

$$J'_n(x) = \frac{1}{2}\left(J_{n-1}(x) - J_{n+1}(x)\right) \quad (29)$$

$$H'_n(x) = \frac{1}{2}\left(H_{n-1}(x) - H_{n+1}(x)\right) \quad (30)$$

After A_m and B_m are calculated using equations (27) and (28), the result can be substituted into equation (21) to obtain the electric field or into equations (23) and (24) to obtain the magnetic field for a vertically polarized line source near a lossy cylinder.

IV. Point Source

Section III derived the electric and magnetic fields due to a line source near a lossy cylinder. This section will convert this line source to a point source to more accurately represent a small body-worn antenna. To perform this transformation, we can take advantage of the following Fourier transform pair:

$$\delta(z - z_0) = \frac{1}{2\pi}\int_{-\infty}^{\infty} e^{-jk_z z}e^{jk_z z_0}dk_z \quad (31)$$

Since the excitation can be written as a superposition of spectral components (integral versus k_z), then the field can also be written as a superposition of such components since the system is linear. This leads to the following integral along k_z:

$$E_{z,TOT} = \frac{1}{2\pi}\int_{-\infty}^{\infty} E_z e^{jk_z z_0}dk_z \quad (32)$$

where $E_{z,TOT}$ is the total electric field due to a point source, and E_z is the z component of the electric field due to a line source given in equation (21). Thus, the field due to a point

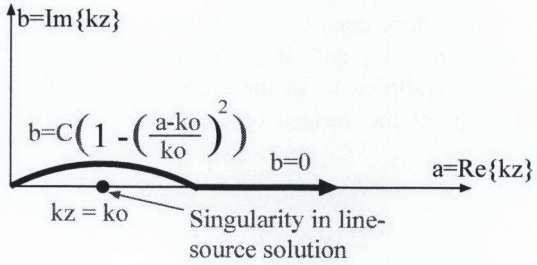

Fig. 4. A parabolic contour integral around the singularity at $k_z = k_0$ is a good numerical method for evaluating the inverse Fourier transform needed to obtain the solution for a point source.

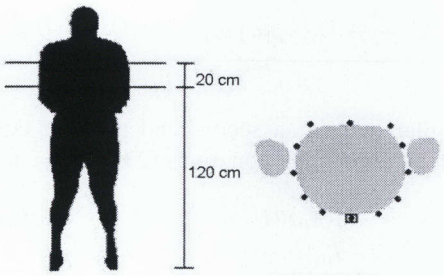

Fig. 5. Measurement positions taken around a human torso in an anechoic chamber.

source can be computed by summing together the fields due to an infinite number of line sources with currents $e^{-jk_z z}$.

The integration in equation (32) must be performed numerically using a contour integral in the complex plane to avoid a singularity in E_z when k_z is equal to the free-space wave number k_0 (see Figure 4). We have found that a parabolic contour defined as in Figure 4 together with Simpson's Rule, suitable for parabolic functions, provides a practical numerical integration technique that rapidly converges to a good approximation of the solution.

V. Comparison with Measurements

Obviously, the geometry considered in the previous sections does not perfectly represent an antenna and body. Thus, we have compared our simplified model with measurements of the electric field close to the human body using actual antennas. Section V-A describes our measurement setup, while Section V-B compares our model and measurement results.

A. Measurement setup

An HP8753ES vector network analyzer (VNA) is used to measure the S21 parameter between two antennas placed at various positions on a human body in an anechoic chamber. The two antennas are connected to the VNA using 6 meter low-loss coaxial cables. Measurements are taken at 915 MHz and 2.45 GHz.

The same small, low-profile Skycross SMT-8TO25-MA [17] antennas are used for all measurements. The antennas are 50.5 by 28 by 8 mm in size and weigh only 4.2 grams. These antennas were chosen since they are close to the size and profile requirements typical of comfortable body worn sensor devices [1]. Furthermore, they have a wide bandwidth which minimizes degradation resulting from the antenna being detuned when placed near the body [18].

The distance between the body and the antenna can significantly influence the pathloss and needs to be carefully controlled [3]. We control this separation by putting a 5 mm dielectric between the body and the antenna. In the same manner as [9], the antenna is taped to this dielectric and held against the body using tight elastics so they can not move while a measurement is being made. In all cases, the antennas are mounted so they are vertically polarized parallel to the body surface.

We analyze the antenna matching by measuring the S11 parameter in free-space and close to the body. In free space, the S11 parameter is below -10 dB across the band of interest indicating the measurement setup itself does not introduce significant loss. When mounted on the body, the S11 parameter can vary depending on the placement of the antenna on the body. It remains good at 915 MHz (S11 $<$ -10 dB) but in some cases becomes marginal at 2.4 GHz (S11 $<$ -5 dB). It is possible that the coaxial cable and connector may influence antenna parameters. However, the display on our VNA remains stable when we move the cables indicating they do not radiate enough energy to appreciably alter our results.

Figure 5 shows where the antennas are placed on the body. All channel parameters are extracted from measurements performed in 2 planes separated by 20 cm along the vertical axis (see left diagram). The right diagram shows where the antennas are placed for each plane. The receiver positions are marked with circles, while the transmitter is marked with a box around the circle. The transmitter is always placed on the front, and the receiver is placed at distances of 10, 15, 20, 25, 30, and 40 cm measured around the perimeter of the body.

B. Measurement and model comparison

Figures 6 and 7 compare measurement and model results for 900 MHz and 2450 MHz respectively. The circles represent the S21 measurements taken at various positions around the body as shown in Figure 5. The dashed line connects the mean pathloss in the log domain at each measured distance. The solid line is calculated based on our analytical model developed in Sections III and IV. We have assumed a radius of 13.3 centimeters which roughly corresponds to the average radius of the body used in our measurements. We further assume the lossy cylinder has a conductivity of $\sigma = 0.94294$ S/m at 915 MHz and $\sigma = 1.7388$ S/m at 2450 MHz, and a relative permittivity of $\epsilon = 55.032$ at 915 MHz and $\epsilon = 52.729$ at 2450 MHz. This roughly corresponds to the dielectric properties of muscle tissue [19].

There is a large variance in the pathloss measured at a particular distance around the torso consistent with other measured and simulated results [8], [9]. This variance can be attributed to several physical factors including random interaction of the antenna and body at different locations, reflections off the arms or floor, and variations in the local curvature or tissue properties. Furthermore, distance measurements made on a body are only accurate to about ± 1 centimeters which can also contribute to this variance. Since our analytical model is based on a uniform lossy cylinder and does not incorporate antenna losses, we can not expect it to take into account these fluctuations. Some researchers have proposed to model these contributions using a log-normal random variable since many of the effects are multiplicative [8], [10].

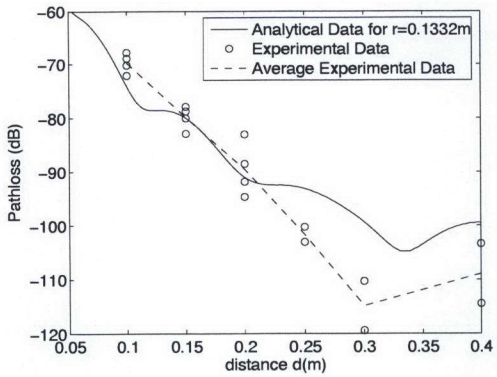

Fig. 6. Pathloss versus distance measured around the body at a frequency of 915 MHz.

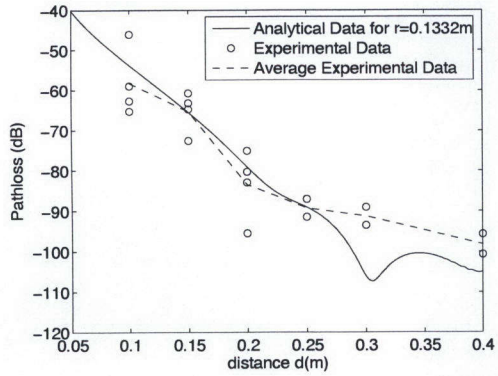

Fig. 7. Pathloss versus distance measured around the body at a frequency of 2450 MHz

Comparison of the dashed and solid curves indicates that the analytical model provides a good approximation of the average pathloss trends around the body, particularly on the front and sides. Furthermore, it accurately predicts a change of slope in the pathloss around the back of the body which has been observed in several other studies [7]–[9]. This change in slope can be at least partially attributed to clock-wise and counter-clockwise waves combining on the backside of the body, though the situation is likely more complicated at lower frequency where some penetration through the body is expected.

Comparison of the dashed and solid lines indicate that the model may be less accurate when antennas are located on opposite sides of the body. One possible explanation is that some effects not incorporated in our model, such as arm and ground reflections, play a larger role when the antennas are on opposite sides of the body. This explanation makes physical sense and has been suggested in some studies [2], [3], [20]. However, we also note that less measurements were taken on the back side of the body. Given the large variance of the measured results, it is possible that our estimate of the average pathloss versus distance (the dashed line) is simply less accurate in this region.

VI. Conclusions and Future Work

We have proposed a generic approach to understanding body area propagation by modeling the body as a lossy cylinder and the antennas as a point source. Since this approach is derived directly from fundamental principles and can be extended to all frequencies and polarities, it well compliments existing numerical and measured statistical models which are limited in scope and are not always physically motivated. To predict the fields for this arrangement, we propose a two step procedure. First, the well-known solution for a line-source near a lossy cylinder can be derived using the addition theorem for Hankel functions. Second, the line-source is converted to a point source by taking the inverse Fourier transform of the line source solution. To demonstrate this procedure, we have derived the solution for a vertically polarized line source. We then proposed a parabolic contour integral to convert this solution to a point source. We have compared the resulting model with measurements taken around the surface of the body. The model accurately predicts the average pathloss trends in most cases. However, more measurements are needed to determine the accuracy of our model when antennas are located on opposite sides of the body.

While the approach presented here is general, we have only presented results for a vertically polarized point source. Furthermore, we have simplified this problem by ignoring the $\hat{\phi}$ and $\hat{\rho}$ components of the electric field. In the future, we will present a complete solution to the problem incorporating all field components. Furthermore, we will consider other antenna polarities and make additional anechoic chamber measurements.

References

[1] B. Gyselinckx, C. Van Hoof, S. Donnay, "Body area networks, the ascent of autonomous wireless microsystems," in *International Symposium on Hardware Technology Drivers of Ambient Intelligence*, 2004.

[2] T. Zasowski, F. Althaus, M. Stager, A. Wittneben, and G. Trőster, "UWB for noninvasive wireless body area networks: channel measurements and results," in *2003 IEEE Conference on Ultra Wideband Systems and Technologies*, 2003, pp. 285–289.

[3] A. Fort, C. Desset, J. Ryckaert, P. De Doncker, L. Van Biesen, and P. Wambacq, "Characterization of the ultra wideband body area propagation channel," in *ICU Proceedings*, Zurich, 2005.

[4] P. Hall, M. Ricci, and T. Hee, "Measurements of on-body propagation characteristics," in *International Conference on Microwave and Millimeter Wave Technology*, 2002, pp. 770–772.

[5] A. Alomainy, Y. Hao, X. Hu, C. G. Parini, and P. S. Hall, "UWB on-body radio propagation and system modelling for wireless body-centric networks," in *IEE Communications Proceedings*, vol. 153, no. 1, February 2006, pp. 107–114.

[6] W. Scanlon and N. Evans, "Numerical analysis of bodyworn UHF antenna systems," *Electronics and Communication Engineering Journal*, vol. 13, no. 2, pp. 53–64, 2001.

[7] J. Ryckaert, P. DeDoncker, S. Donnay, A. Delehoye, and R.Meys, "Channel model for wireless communication around the human body," in *Electronics letters*, vol. 40, no. 9, April, pp. 543–544.

[8] Y. Zhao, Y. Hao, A. Alomainy, and C. Parini, "UWB on-body radio channel modeling using ray theory and subband FDTD method," vol. 54, no. 4, pp. 1827–1835, June 2006.

[9] A. Fort, J. Ryckaert, C. Desset, P. De Doncker, and L. Van Biesen, "Ultra wideband channel model for communication around the human body," *IEEE Journal on Selected Areas of Communication*, 2006.

[10] A. Fort, C. Desset, P. De Doncker, and L. Van Biesen, "An ultra wideband body area propagation channel model: From statistics to implementation," *IEEE Transactions on Microwave Theory and Techniques*, 2006.

[11] Andreas F. Molisch et al., "A comprehensive standardized model for ultrawideband propagation channels," *IEEE Transactions on Antennas and propagation*, vol. 54, no. 11, pp. 3151–3166, November 2006.

[12] A. Fort, C. Desset, P. Wambacq, , and L. Van Biesen, "Body area RAKE receiver communication," in *IEEE Conference on Communications (ICC)*, Turkey, 2006, pp. 4682–4687.

[13] A. Fort, M. Chen, C. Desset, P. Wambacq, , and L. Van Biesen, "Impact of sampling jitter on mostly-digital architectures for UWB bio-medical applications," in *IEEE Conference on Communications (ICC)*, Glascow, 2007.

[14] D. A. Mcnamara, C. Pistorius, and J. Malherbe, *Introduction to the uniform geometrical theory of diffraction*. Artech House: Boston, 1991.
[15] W. C. Chew, *Waves and fields in inhomogeneous media*. New York: IEEE Press, 1995.
[16] A. Morse and M. Feshbach, *Methods of Theoretical Physics*. New York: MacGraw-Hill, 1979.
[17] Skycross, http://www.skycross.com.
[18] W. G. Scanlon, N. E. Evans, and M. Rollins, "Antenna-body interaction effects in a 418 mhz radio telemeter for infant use," in *18th Annual International Conference of the IEEE Engineering in Medicine and Biology Society*, 1996, pp. 278–279.
[19] C. Gabriel, "Compilation of the dielectric properties of body tissues at RF and microwave frequencies," Brooks Air Force, Technical Report AL/OE-TR-1996-0037, 1996.
[20] A. Fort, C. Desset, J. Ryckaert, P. DeDoncker, L. Van Biesen, and S. Donnay, "Ultra wide-band body area channel model," in *ICC Proceedings*, Seoul, Korea, 2005.